UG-DFM-3/97
nucl-th/9704022

Radiative pion capture in nuclei: a continuum shell–model approach

J.E. Amaro, A.M. Lallena and J. Nieves

Departamento de Física Moderna, Universidad de Granada,
E-18071 Granada, Spain

Abstract

The radiative pion capture process in nuclei is approached by using a continuum shell–model description of the nucleus, together with a phenomenological treatment of the two particle–two hole effects. It is found that these effects play an important role to reproduce the observed experimental photon energy distribution. This distribution as well as the integrated one depends significantly on the details of the mean field potential. This makes this process interesting to investigate the nuclear structure dynamics.

PACS: 25.90.+k, 36.10.Gv
Keywords: Radiative pion capture, final state interactions, two particle–two hole correlations, continuum shell–model.

1 Introduction

The radiative pion capture (RPC) in pionic atoms has been extensively studied in the past [1]-[5]. In this process, the π^- sited in a given nl orbit of a pionic atom is captured by the nucleus emitting a photon. The interest of this reaction is threefold. First, it provides direct information about the π-nucleus interaction, responsible for the formation of the pionic bound state. Second, it proves the nuclear structure, specifically the details of the proton-distribution, and the nature of the two particle–two hole ($2p2h$) effects in the nuclear medium. Finally, it gives valuable information on the $\pi^- p \rightarrow \gamma n$ reaction on the nucleon at very low pion kinetic energies and in this sense it is complementary to the pion photoproduction reactions. In this paper we will concentrate on the second aspect mentioned above.

Technically, the most difficult aspect in the theoretical side is the evaluation of the sum over final nuclear states. This has made necessary the use of different approaches such us the closure approximation [4] or the RPA sum rules [5]. In the first case, the results show a considerable dependence on the average photon energy used, a problem which is minimized by the RPA sum rules method. However, this two approximations only give integrated quantities (e.g. the radiative capture widths and branching ratios), but observables such as the photon energy distribution are out of their possibilities.

More recently, Chiang *et al.* [6] have proposed a many–body approach in which both the photon energy distribution and the radiative capture width can be calculated. Starting from techniques developed for the (γ, π) reaction [7], this method permits the use of accurate pionic wave functions and the incorporation of the medium polarization effects. Besides, the calculations are considerably simplified because they are done in infinite nuclear matter and applied to finite nuclei by means of the local density approximation (LDA). Though the obtained branching ratios and widths are in overall agreement with the experimental results, the photon energy distribution does not show the marked tail of the data at low photon energies. This last problem is partially due to the limited momentum components available to the nuclear wave functions obtained from the Fermi gas (FG) model.

Shell–model (SM) calculations do not present this deficiency. This was observed in the pioneering work of Vergados [1] and Eramzhyam *et al.* [8] and in the results obtained by Ohtsuka and Ohtsubo [9] and Wünsch [10] within the continuum SM approach. Much of this work has been devoted to the analysis of the role played by the resonances in the reaction and the main conclusion is that the RPC can be described assuming a dominant resonance character for the process.

In this work we want to investigate the dynamics of the RPC reaction in more detail by analyzing it with a continuum SM recently developed to study the quasi–free inclusive electron scattering by nuclei [11, 12]. In particular we want to address different questions related to the importance of the parameters of the SM potential, to the problem of the orthogonality of the single–particle wave functions and to the effect of the inclusion of the particle–hole (ph) self–energy in the medium on the ph propagator. This latter effect

accounts for the final state interactions (FSI) of the emitted neutron with the residual nucleus.

The organization of the paper is as follows. In sect. 2 we give the details of the model used to perform the calculations with the explicit expressions of the necessary matrix elements placed in the appendix. In sect. 3 we show the results and comment the main features. In sect. 4 we summarize our work and draw our conclusions.

2 Details of the model

2.1 The RPC rate

In this work we study the following reaction:

$$\left({}^{A}_{Z}\mathrm{X}_N + \pi^-\right)_{\mathrm{bound}} \rightarrow \gamma + n + {}^{A-1}_{Z-1}\mathrm{Y}_N \tag{1}$$

where the pion is captured by the nucleus emitting a neutron and a photon, being the latter one the only particle detected.

The unpolarized differential photon distribution for the capture of a pion, bound in the orbit nl, from a spin zero nucleus is given by [13]:

$$\frac{d\Gamma^{(\gamma)}_{nl}}{dq}(q) = \frac{8\pi\alpha q}{2J_i+1}\sum_{fJ}\delta(q+E_f-E_i)\left[|\langle f\|T^{\mathrm{el}}_J(q)\|i\rangle|^2 + |\langle f\|T^{\mathrm{mag}}_J(q)\|i\rangle|^2\right]. \tag{2}$$

Here it has been taken into account the fact that the nuclear states as well as that of the pion have good angular momenta, what makes useful to perform a multipole expansion of the operators involved. In Eq. (2), α is the fine structure constant, q is the energy of the emitted photon, $|i\rangle$ and $|f\rangle$ represent the initial (taking into account the pion degrees of freedom) and final hadronic states of the system and $E_{i,f}$ are their respective energies. Besides, T^{el}_{JM} and T^{mag}_{JM} are the electric and magnetic multipole operators which are given by:

$$T^{\mathrm{el}}_{JM}(q) = \frac{1}{q}\int \mathrm{d}^3r\,\left\{\nabla\times\left[j_J(qr)\,\mathbf{Y}^M_{JJ}(\hat{\mathbf{r}})\right]\right\}\cdot\mathbf{J}(\mathbf{r}), \tag{3}$$

$$T^{\mathrm{mag}}_{JM}(q) = \int \mathrm{d}^3r\, j_J(qr)\,\mathbf{Y}^M_{JJ}(\hat{\mathbf{r}})\cdot\mathbf{J}(\mathbf{r}), \tag{4}$$

where j_J is a spherical Bessel function and $\mathbf{Y}^M_{JL}$ a vector spherical harmonic. Finally, $\mathbf{J}(\mathbf{r})$ is the electromagnetic current operator.

The amplitude for the elementary process $\pi^- p \rightarrow \gamma n$, which determines the hadronic current, depends [14] on the spin of the nucleon involved in the process, the photon polarization and the pion and photon momenta. However, the average momentum of the

bound pion in light and medium nuclei is small and in this situation it is plausible to take into account only the so–called Kroll–Ruderman term (which is the one surviving in the limit of zero pion momentum). Then we have for the electromagnetic current operator

$$\mathbf{J}(\mathbf{r}) \;=\; i\sqrt{2}\,\frac{f}{m_\pi}\,\left(1+\frac{m_\pi}{2M}\right)\,\sum_{i=1}^{A}\,t_-(i)\,\phi_-(\mathbf{r})\,\boldsymbol{\sigma}(i)\delta(\mathbf{r}-\mathbf{r}_i). \tag{5}$$

Here, the index i runs over the A nucleons of the system with coordinates $\mathbf{r}_i$, f is the pion–nucleon coupling constant ($f^2/4\pi = 0.08$), m_π is the pion mass, M is the nucleon mass and $\boldsymbol{\sigma}$ are spin Pauli matrices. Besides, the isospin operator t_- transforms a proton into a neutron. Finally, $\phi_-(\mathbf{r})$ is the pion field operator which can be developed in a complete basis as follows:

$$\phi_-(\mathbf{r}) \;=\; \sum_k\,\frac{1}{\sqrt{2E_k^\pi}}\,\phi_k(\mathbf{r})\,c_k, \tag{6}$$

where k runs over all the pionic atom orbits, ϕ_k is the corresponding pion wave function, c_k is the pion annihilation operator, and E_k^π is the pion energy including its mass.

After substituting the current (5) in Eqs. (3) and (4) it is possible to obtain the tensor form of these electromagnetic operators and calculate the matrix elements involved in Eq. (2). These expressions can be found in the Appendix.

2.2 The model of nuclear structure

The matrix elements in Eq. (2) require the definition of the initial and final states of the system. We are dealing with closed–shell nuclei and then our initial state is built by coupling the π^- atomic wave function with the closed–shell core. Thus the initial state is given by:

$$|i\rangle \equiv |J_iM_i\rangle \;=\; \left[|\pi^-;nl\rangle\otimes|0^+\rangle\right]^{J_i}_{M_i} \tag{7}$$

with $J_i = l$ and $|0^+\rangle$ the Slater determinant corresponding to the closed–shell nucleus. The Slater determinant is built with single–particle wave functions obtained by diagonalizing a Woods–Saxon potential well

$$V_{\rm Woods-Saxon}(r) = V_0 f(r,R_0,a_0) + V_{LS}\frac{\mathbf{l}\cdot\boldsymbol{\sigma}}{r}\frac{df(r,R_{LS},a_{LS})}{dr} + V_C(r), \tag{8}$$

where

$$f(r,R,a) = \frac{1}{1+\exp\left(\frac{r-R}{a}\right)} \tag{9}$$

and $V_C(r)$ is the Coulomb potential created by an homogeneous charge distribution of radius R_C. The parameters of this potential are adjusted to reproduce different nuclear properties such as, e.g., the experimental single–particle energies around the Fermi level, the r.m.s. radius or the charge density [15]. On the other hand the pion state, $|\pi^-;nlm_l\rangle$, is defined as follows:

$$\phi_-(\mathbf{r})\,|\pi^-;nlm_l\rangle \;=\; \frac{1}{\sqrt{2E_{nl}^\pi}}R_{nl}^\pi(r)\,Y_{lm_l}(\hat{\mathbf{r}})|0\rangle_\pi \tag{10}$$

with $|0\rangle_\pi$ the pion vacuum state, n, l and m the principal, orbital angular momentum and magnetic quantum numbers of the pion atomic orbit and $Y_{lm}(\hat{\mathbf{r}})$ spherical harmonic functions. The radial pion wave function $R^\pi_{nl}(r)$ and the pion energy E^π_{nl} are obtained by solving the Klein-Gordon equation with a pion-nucleus optical potential. This potential has been developed microscopically and it is exposed in detail in Ref. [16] for pionic atoms. It contains the coulombian π^-- nucleus interaction and the ordinary lowest order optical potential constructed from the s– and p–wave πN amplitudes. In addition second order terms in both s– and p–waves, responsible for pion absorption, are also considered. Standard corrections to both the electromagnetic (finite size of the nucleus and vacuum polarization) and strong (second-order Pauli re-scattering term, ATT term, Lorentz–Lorenz effect, long and short range nuclear correlations) parts of the potential are also taken into account. This theoretical potential reproduces fairly well the data of pionic atoms (binding energies and strong absorption widths) [16] and low energy π-nucleus scattering [17].

In Eq. (2), the initial energy E_i corresponds to the energy of the $(\pi X)_{\rm bound}$ system, including the pion binding energy. As we are only interested in the excitation nuclear energy, we take the energy of the initial closed–shell nucleus as our zero of energies. Thus the initial energy E_i can be identified as the pion mass plus its binding energy, E^π_{nl}.

The final states are described in terms of a neutron particle in the continuum and a proton hole coupled to the final angular momentum J_f,

$$|f\rangle \equiv |ph^{-1}; J_f M_f\rangle = \left[a^\dagger_p \otimes b^\dagger_h\right]^{J_f}_{M_f} |0^+\rangle \tag{11}$$

where $a^\dagger_p$ ($b^\dagger_h$) is the particle (hole) creation operator. The particle states are obtained by solving the Schrödinger equation for positive energies. We have used the same Woods–Saxon potential as for the discrete single–particle levels in order to ensure the orthogonality of the states involved in the process (see Ref. [11] for details). It is important to mention here that, in view of the definition of the final states we are using, the sum over final states $|f\rangle$ in Eq. (2) should be changed to:

$$\sum_f \longrightarrow \sum_{ph} \sum_{J_f}. \tag{12}$$

Therefore, to evaluate Eq. (2) we must perform a sum over the quantum numbers of the final particle-hole states ($h = n_h, l_h, j_h$, $p = \epsilon_p, l_p, j_p$ and the total angular momentum J_f of the ph excitation) and the photon angular momentum (J). The sum over ϵ_p is indeed an integration which is performed by means of the delta of energies which appears in Eq. (2). Actually, in our model, the final energy E_f is given by

$$E_f = \Delta m + \epsilon_p - \epsilon_h, \tag{13}$$

with ϵ_α the energy of the single–level α and Δm the difference between the masses of the particle (neutron) and hole (proton) nucleons. Thus, for each value of the photon energy q and each hole h, ϵ_p is univocally determined by the delta function in Eq. (2).

Nucleus	Shell	$\epsilon_h(th)$	ϵ_h (exp)
^{12}C	$1p_{3/2}$	-18.05	-15.96
^{16}O	$1p_{1/2}$	-12.74	-12.12
	$1p_{3/2}$	-16.92	-18.45
^{40}Ca	$2s_{1/2}$	-10.30	-10.85
	$1d_{3/2}$	-8.71	-8.33
	$1d_{5/2}$	-16.19	-12.27

Table 1: Proton hole single-particle energies (MeV). We show the theoretical energies computed with the SM potential described in sect. 2.2 (third column) and the experimental ones (fourth column). For more details, see Ref. [15].

Note also that the sum over the photon multipoles, J, ranges from one to infinity. The larger is the photon energy or the nuclear mass, the bigger is the number of photon multipoles needed to obtain convergence. In the RPC process, the maximum photon energy is around the pion mass and we have found in ^{40}Ca a good convergence with four or five multipoles.

One final detail concerns to the hole-energies used in our calculation. As it was mentioned above, our mean-field potential has been adjusted to reproduce single-particle energies around the Fermi level. To improve the energetic balance in our model, in the actual calculation the experimental proton single-particle energies values, when known, have been used. In Table 1, we compare these values to the computed mean-field proton hole energies.

2.3 Effects of the $2p2h$ correlations.

In sect. 2.2, we have outlined our continuum SM approach to the nuclear structure. In this framework, the final state interactions (FSI) of the outgoing particle (neutron) with the residual nucleus are partially taken into account. However, $2p2h$ correlations are a fundamental ingredient to achieve a reasonable descriptions of these FSI. Here, we discuss briefly the phenomenological model for such effects used in this work. We follow the approach of Ref. [18]. There, the propagation of the mean field ph excitations in the nuclear medium is modified by including an approximated complex ph self–energy. This self–energy is determined by the effective nucleon-nucleon residual interaction in the medium not included in the mean field approach. The inclusion of the $2p2h$ correlations improves our treatment of the FSI and it also accounts for corrections to the pure one–body RPC due to two nucleons mechanisms. This approach has proved to be successful in the study of the transverse [12] and longitudinal [19] response functions in the quasielastic region for inclusive (e, e') processes. Also a recent approach [20], where the propagation of ph excitations in the medium is described in terms of particle and hole spectral functions gives similar results to those of Refs. [12] and [19].

In previous approaches [1], FSI were taken into account by putting the outgoing neutron in a wave of an neutron-nucleus optical potential. The imaginary part of the optical potential reduces the outgoing neutron flux and therefore reduces the integrated RPC rate. However, we believe this procedure is incomplete: the imaginary part of the optical potential is mainly due to two–body mechanisms which also contribute to the RPC rate and have to be considered in order to be consistent (see Ref. [6] for more details). Our approach, where we incorporate a *ph* self–energy, automatically takes into account both physical processes mentioned above, leading to a redistribution of the strength of the differential photon rate but as we shall see leaving the integrated RPC rate almost unchanged.

Following the steps of Ref. [19] to include the $2p2h$ correlation effects to the RPC differential rate, one should fold the pure one body SM differential rate, $\left(d\Gamma_{nl}^{(\gamma)}(q)/dq\right)^0$, given in Eq. (2), with the electromagnetic current and final states defined in Eqs.(5) and (11), with the imaginary part of the *ph* propagator:

$$\frac{d\Gamma_{nl}^{(\gamma)}(q)}{dq} = \int_0^{m_\pi} dq' \left(\frac{d\Gamma_{nl}^{(\gamma)}(q')}{dq'}\right)^0 \left[\rho(m_\pi - q', m_\pi - q) + \rho(m_\pi - q', q - m_\pi)\right] \quad (14)$$

with

$$\rho(E,\omega) = \frac{1}{2\pi}\frac{\Gamma^{\downarrow}(\omega)}{(E-\omega-\Delta(\omega))^2 + (\Gamma^{\downarrow}(\omega)/2)^2}. \quad (15)$$

The functions $\Delta(\omega)$ and $\Gamma^{\downarrow}(\omega)$ define the complex self–energy,

$$\Sigma(\omega) = \Delta(\omega) - \frac{i}{2}\Gamma^{\downarrow}(\omega) \quad (16)$$

of a *ph* with excitation energy ω. The self–energy $\Sigma(\omega)$ has been taken from Ref. [19].

3 Results

In this section we apply our model to calculate the RPC differential rates for three closed–shell medium nuclei, ^{12}C, ^{16}O and ^{40}Ca, and compare our predictions with the available experimental data.

Experimentally, it is rather difficult to distinguish between RPC processes from different pionic atom orbits. Indeed, only the weighted ratio

$$\frac{dR^{(\gamma)}}{dq} = \sum_{nl} \frac{\omega_{nl}}{\Gamma_{nl}^{abs}} \frac{d\Gamma_{nl}^{(\gamma)}}{dq} \quad (17)$$

can be measured. Here, ω_{nl} gives the absorption probability from each nl pionic level, taken into account the electromagnetic transitions and the strong absorption, and are normalized to the unity. Γ_{nl}^{abs} is the total pion absorption width from the orbit nl and

Nucleus	nl	ω_{nl}	Γ_{nl}^{abs} (KeV)
^{12}C	$1s$	0.1	3.14
	$2p$	0.9	0.00136
^{16}O	$1s$	0.1	7.92
	$2p$	0.9	0.00676
^{40}Ca	$2p$	0.7	1.59
	$3d$	0.3	0.0007

Table 2: Values of ω_{nl} [2] and Γ_{nl}^{abs} [21]—[25] used in this work.

$\Gamma_{nl}^{(\gamma)}$ is the width due to the radiative capture of the pion from the orbit nl. As disccused in [2], we make the approximation of putting all the weight of radiative capture in the two pionic levels observed with the X-ray technique. The values used in this work for these parameters are shown in Table 2. In what follows we will refer to $dR^{(\gamma)}/dq$ instead of the single differential decay rate of Eq. (2).

We start now discussing our results. Firstly, we focus on the purely one-body process and later we will introduce the effects of the $2p2h$ correlations. In Fig. 1, we show the contribution to $dR^{(\gamma)}/dq$ from the different holes configurations in ^{12}C, ^{16}O and ^{40}Ca. The most important contributions are due to the $1p$ shell in ^{12}C and ^{16}O and to the $1d$ and $2s$ shells in ^{40}Ca. In all cases they correspond to the outest hole configurations, which maximize the overlap with the pion wave function. The end of the contribution of a particular shell produces a protuberance in the total sum. On the other hand, in the plots also appear resonance structures, specially in ^{40}Ca where turn out to be extremely narrow with typical widths of the order of 10 KeV. This was already pointed out in [26]. However, the resonance structure for low nuclear excitation energies depends strongly on the details of the potential. The use of a different nuclear structure model will produce drastic changes of both their widths and positions.

Note also that in the data, these resonances will be convoluted with the experimental photon energy resolution, which is much greater than their widths and therefore the sharp resonances shapes will smear out and a smoother spectrum will be observed. Here, we are mainly interested in the global shape of the photon distribution and the study of these fine details is out of the scope of this work, because it will require both a more refined nuclear model and more precise experimental data.

In Fig. 2 we compare the total sum of all hole contributions shown in Fig. 1 with the experimental data. In calcium and oxigen, following the discussion above, we have eliminated the sharp resonance structures in our differential rates by convoluting the responses with a Gaussian weight function $f(\omega) \propto exp(-\omega^2/\Gamma^2)$ of width $\Gamma = 1.5$MeV. This convolution procedure keeps unchanged the integrated RPC rate [27]. The experimental data are given in arbitrary units, thus to compare with the experiment we have normalized our results to the data at $q = 105$ MeV. The reason to normalize our results in this region of intermediate energies is twofold. Firstly because is far from the low nuclear excitation energy region (high photon energies) where, as we discuss above, the theoretical results

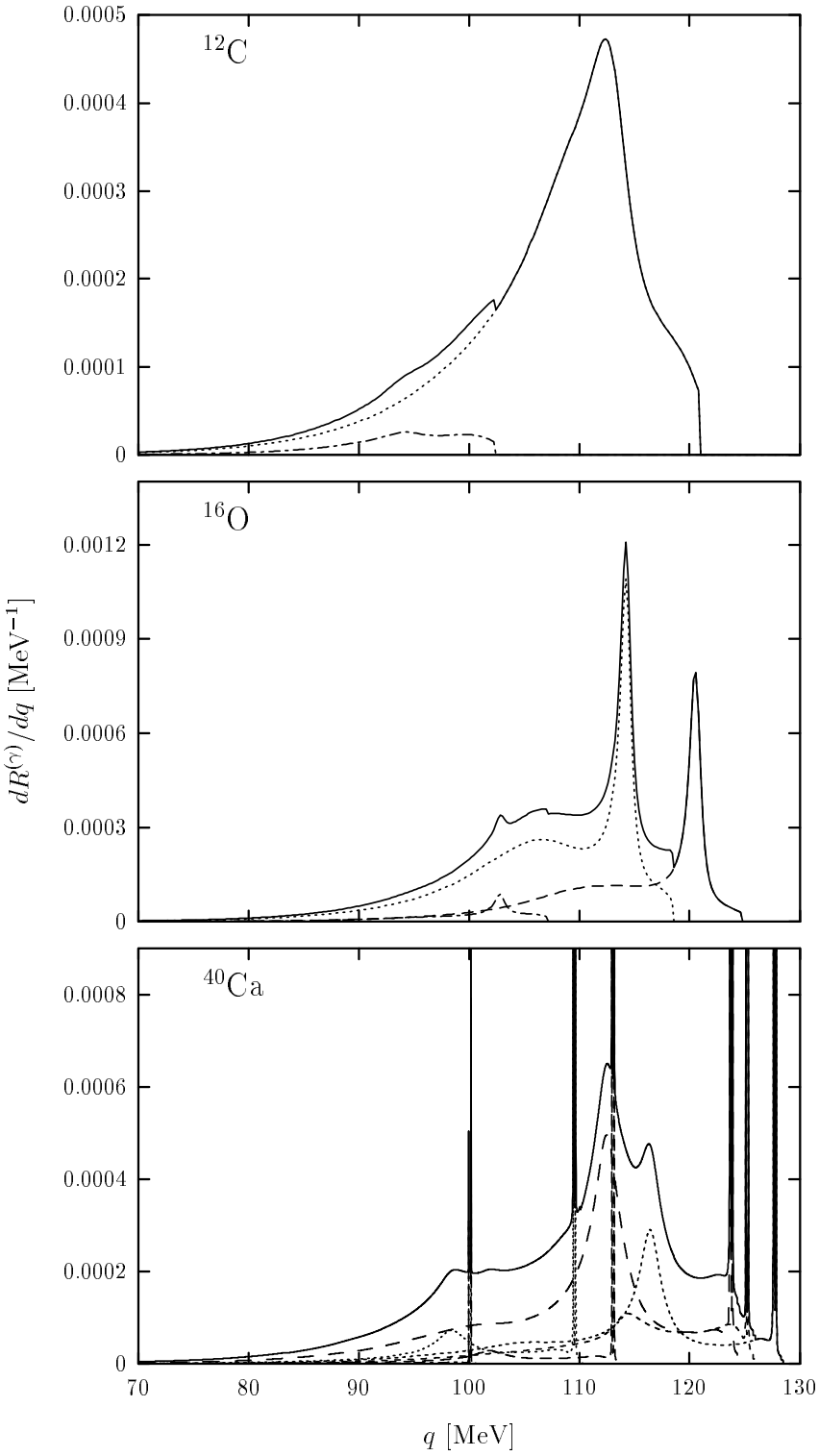

Figure 1: Contribution to $dR^{(\gamma)}/dq$ from the different holes configurations in ^{12}C, ^{16}O and ^{40}Ca. In all figures, the solid lines stand for the total sum of the contribution of the hole configurations. Each hole can contribute up to a maximum photon energy, $q^{(h)}_{max} = E_i - \Delta m + \epsilon_h$, which is different for each shell. This fact can be used to identify the contribution of each hole in the figures: the deeper is the shell, the smaller is $q^{(h)}_{max}$. From the deepest to the outest shell, the hole configurations involved are: $1s_{1/2}$, $1p_{3/2}$, $1p_{1/2}$, $1d_{5/2}$, $2s_{1/2}$ and $1d_{3/2}$.

Potential	V_0 (protons)	V_0 (neutrons)	$R^{(\gamma)}[\%]$
A	-57.5	-55.0	1.25
B	-50.0	-55.0	1.54
C	-50.0	-50.0	1.87
D	-50.0	-60.0	1.21

Table 3: Different Woods–Saxon potentials considered in this work. The second and third columns give proton and neutron Wood–Saxon well depth parameters (in MeV) for ^{40}Ca used to compute the different curves appearing in Fig. 3. The rest of the parameters, not shown here, are common for all potentials and can be found in Ref. [15]. The potential B has been adjusted to reproduce the experimental proton density, whereas C(D) corresponds to a 10% decrease (increase) of the depth for the neutron Wood-Saxon well. The fourth column gives the integrated ratio $R^{(\gamma)}$ (in percent) for each potential.

depend strongly on the nuclear model. Secondly, because the low photon energy region is sensitive to the high momentum components of the hole wave function, and one expects theoretical uncertainties in the nuclear model. Furthermore, as we will show below, the effect of $2p2h$ correlations should be also included in the low energy photon region.

As it can be seen in Fig. 2 our description gives the gross features of the experimental data. However, at the lower end of the photon spectrum the tail of the theoretical distribution is significantly narrower than the experimental one. Furthermore, at high photon energies, major discrepancies also appear because the contributions there correspond to processes where the outgoing neutron is either bound in the residual nucleus or it is in the continuum but carrying low kinetic energies. The first contributions have not been considered in our approach yet while the latter ones depend strongly on the details of the nuclear structure model.

One may think that the situation could be improved by allowing for reasonable modifications of the mean field potential. In Fig.3 we show the results for $dR^{(\gamma)}/dq$ in ^{40}Ca obtained with the four different potentials defined in Table 3. They differ each other only in the proton or neutron depth of the Wood-Saxon well (parameter V_0 in Eq. (8)). We see in the figure that none of the new potentials (B,C,D) give a photon distribution significantly wider than the A potential, used throughout this work. However, the behavior above 110 MeV (low nuclear excitation energies) turns out to be very sensitive to the potential. The area below the curves depends also appreciably on the model and it increases when the neutron Wood–Saxon depth decreases.

Now we focus our attention in the effects of the $2p2h$ correlations. Following the method described in sect. 2.3, we include the effects of the ph self–energy in the medium, into the pure one–body SM differential rates of Fig. 1. The results are shown in Fig. 4. We find an excellent agreement with the experimental distribution, specially in the low energy tail. Clearly, the inclusion of two body mechanisms has made the distribution wider and turns out to be essential to explain the tail of the experimental data. For comparison we also show the results for ^{40}Ca with the model of Ref. [6]. In this reference,

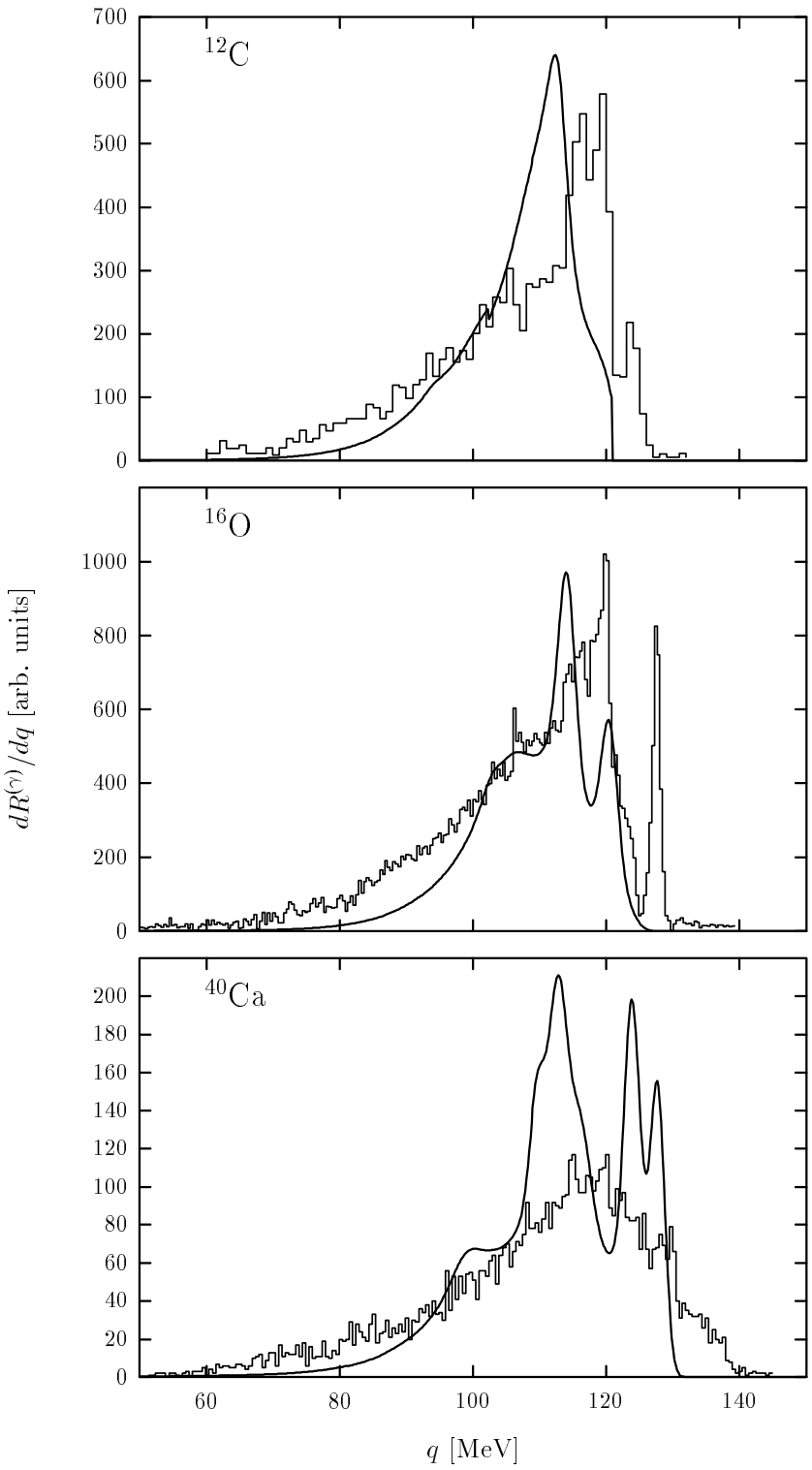

Figure 2: Results for $dR^{(\gamma)}/dq$ in ^{12}C, ^{16}O and ^{40}Ca. Only one-body contributions have been included. Experimental data, taken from [2] and [28], are given in arbitrary units. Our results have been normalized to the data at $q = 105$ MeV. In oxigen and calcium we have convoluted our differential decay rate with a Gaussian weight function of width 1.5 MeV.

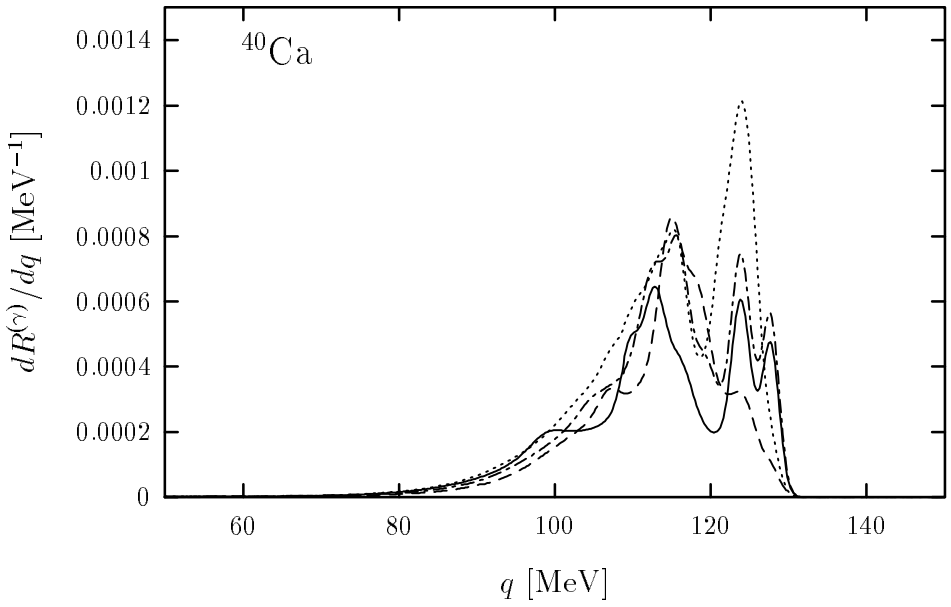

Figure 3: Results for $dR^{(\gamma)}/dq$ in ^{40}Ca with the different SM potentials defined in Table 3. The solid line corresponds to the potential A outlined in sect. 2.2 and used in the rest of this paper. Dash-dotted, dotted and dashed curves correspond to the potentials B,C and D respectively.

the calculations were performed in nuclear matter and the LDA was used to obtain results in finite nuclei. There, though it was found a fair agreement for the integrated ratio $R^{(\gamma)}$ throughout the periodic table, it was pointed out the inability of the model to describe the tail of the photon distribution. In Ref. [6] this problem was associated to the lack of high-momentum components in the FG nucleon wave functions. Here, we show that, in addition to the use of proper nucleon wave functions, one needs to incorporate $2p2h$ correlations to understand the experimental distribution.

To discuss in more detail the effect of the inclusion of ph self–energy in the calculation of the differential decay rate, we show in Fig. 5 the results for $dR^{(\gamma)}/dq$ in ^{16}O with and without the inclusion of $2p2h$ correlations. As it can be seen, these effects reduce the strength of the differential rate in the region of energies around the peak due to the pure one–body absorption, as it would do a FSI treatment with an optical potential. But, in addition these $2p2h$ correlations incorporate the contribution to the RPC process due to two–nucleons mechanisms in the low energy part of the photon spectrum. The net effect is a redistribution of the strength in the spectrum, with a variation of less than 10% in the integrated rate $R^{(\gamma)}$. Similar effects have been also found in inclusive (e, e') processes at the quasielastic [11], [19], [20] and Δ peaks [20] and also in inclusive (p, p') and (n, p) processes [18].

Besides, we would like to stress that the use of the same mean field potential for particle and hole states in our calculations, guarantees the orthogonality of the ph states. It is common in the literature ([1], [10]) to use different potentials for particles and holes (optical models for the particles and mean field potentials for the holes, etc...) and therefore

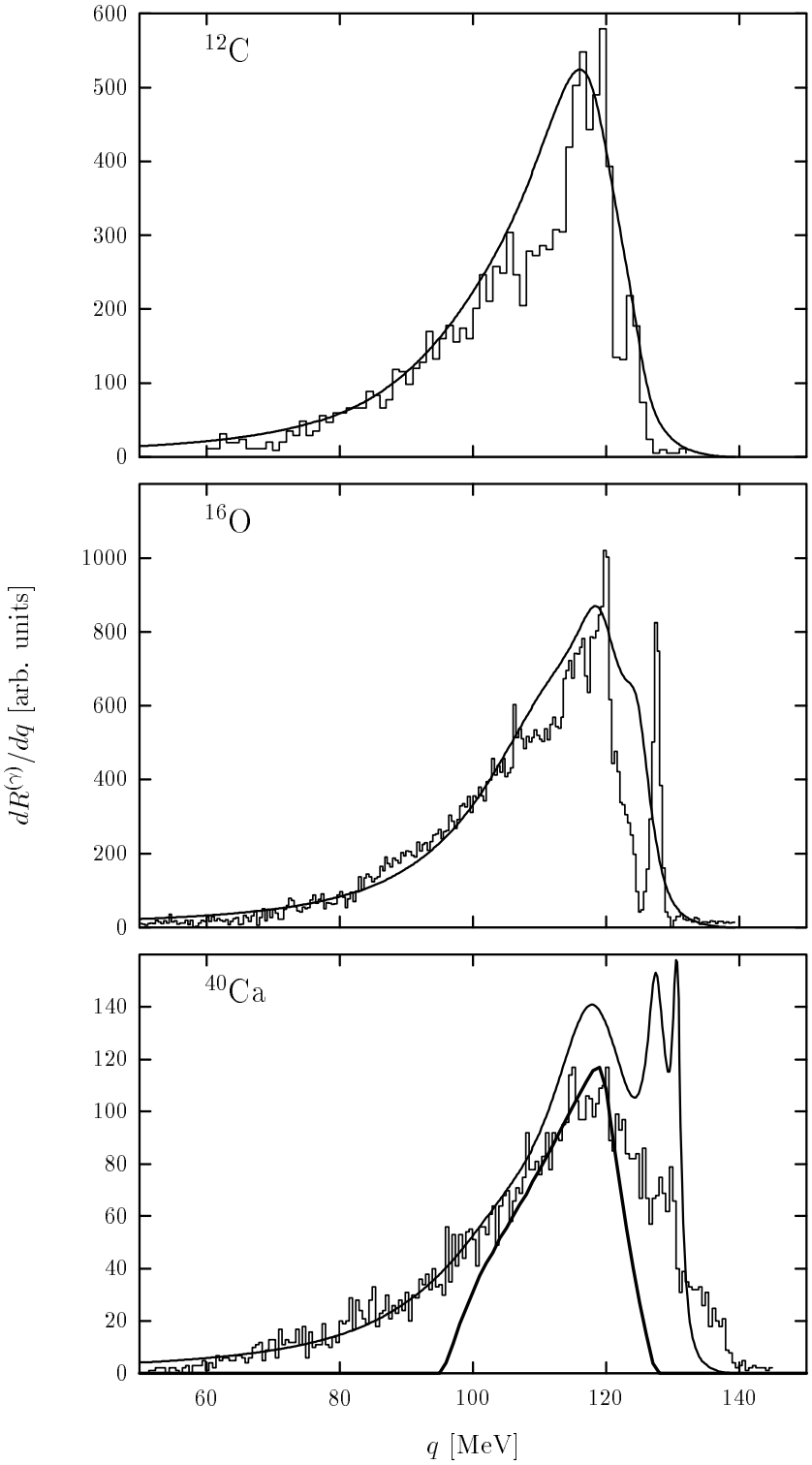

Figure 4: Results for $dR^{(\gamma)}/dq$ in ^{12}C, ^{16}O and ^{40}Ca. Two-body contributions have been now included. Experimental data, taken from [2] and [28], are given in arbitrary units. Our results have been normalized to the data at $q = 105$ MeV. For comparison in ^{40}Ca we have also shown the FG results presented in Fig. (3) of Ref. [6] (thick line). The absolute value of the FG distribution around the peak is about a factor two or three greater than the SM one (thin line) and it has been normalized to the peak of the data. Additionally, the FG curve has been shifted 10 MeV to the left.

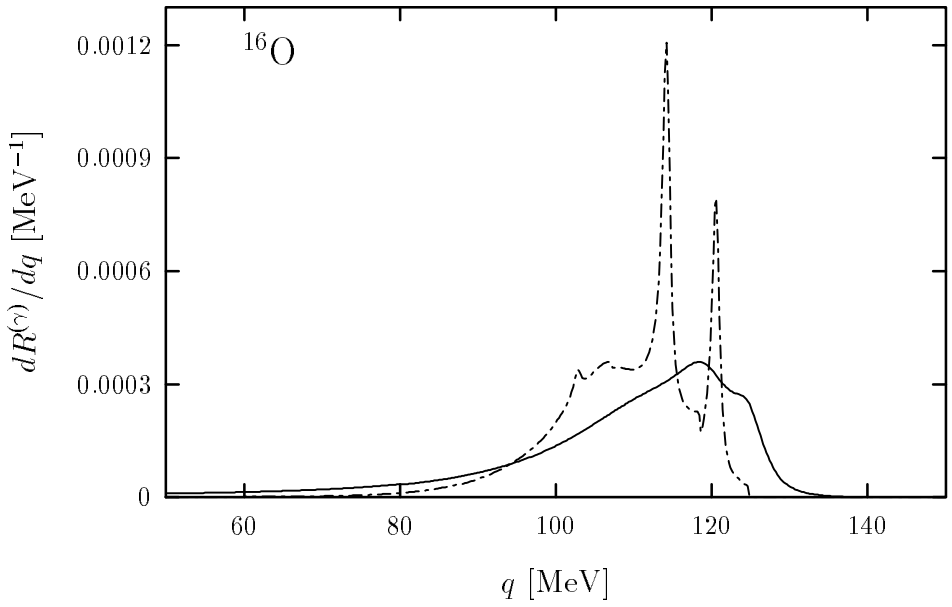

Figure 5: Results for $dR^{(\gamma)}/dq$ in ^{16}O with (solid line) and without (dashed line) the inclusion of $2p2h$ correlation effects. The area below the curves are 9.2×10^{-3} and 9.8×10^{-3} respectively.

the orthogonality between particle and holes states is lost. In these circumstances, there are new contributions to the transition matrix elements coming from the overlap between non-orthogonal wave functions. These new contributions, though not significant for high momentum transfer processes [29], can be important for processes like this where both energy and momentum transfered to the nucleus are small.

The last aspect we want to discuss concerns the integrated ratio $R^{(\gamma)}$. In Table 4 we present our results for this ratio and compare them with experiment and with those of the FG model of Ref. [6].

The results obtained within the framework described up to here (column labeled "Continuum" in the table) turn out to be around a factor of two smaller than the experimental ones and those of Ref. [6]. However, it is worth to point out here that, as shown in Table 3, the integrated rate is rather sensitive to the details of the SM nuclear potential used, and that a small variation of the model could account for such discrepancies. Apart from this point, other possible reasons for the low rates found are the following:

1. We have only considered the Kroll–Ruderman term for the elementary process $\pi^- p \to \gamma n$. The momentum of the pion on its bound orbit though small is not strictly zero, and one should add to the dominant Kroll–Ruderman term new amplitudes proportional to the pion momentum which could increase the integrate RPC rate. In any case these new contributions are not expected to be important enough to explain the disagreement.

	$R^{(\gamma)}$ [%]				
	Ref. [6]	Continuum	Discrete	Total	Experiment
^{12}C	1.19 ± 0.16	0.62	1.17	1.79	1.84 ± 0.08, 1.92 ± 0.19, 1.6 ± 0.1
^{16}O	1.53 ± 0.08	0.92	0.80	1.72	2.27 ± 0.24, 2.24 ± 0.48
^{40}Ca	1.91 ± 0.29	1.17	0.87	2.04	1.82 ± 0.05

Table 4: Results (in percent) for $R^{(\gamma)}(q)$ in ^{12}C, ^{16}O and ^{40}Ca. The second column contains the results obtained with the FG model of Ref. [6]. Our results are given in the next three columns: third column corresponds to the area below the curves in Fig. 4, fourth column gives the contribution of the RPC processes in which the final neutron is bound in the residual nucleus and finally the fifth column is the total rate, sum of the two previous values. Experimental values are taken from references: [28], [30] and [31] for ^{12}C, [28] and [32] for ^{16}O, and [28] for ^{40}Ca.

2. The determination of the weights ω_{nl} (see Table 2) may be subject to theoretical uncertainties. It would be interesting to disentangle experimentally the capture from different pionic atomic states to allow a direct comparison with the theory, free of the assumptions made on the values of ω_{nl} (for more details see Ref. [2]).

3. Pion capture processes where the outgoing neutron is bound in the residual nucleus instead of going to the continuum lead to Dirac's delta peaks in the photon spectrum which also contribute to the integrated ratio $R^{(\gamma)}$ and have not been considered yet. Indeed, one can easily evaluate these contributions by taking into account that the integral over ϵ_p in Eq. (12) is now a discrete sum over the unoccupied single neutron states (see Ref. [15]) and the radial wave function R_p in Eq. (21) corresponds now to the solution of the radial Schrödinger equation for a negative energy ϵ_p.

   In the fourth column of Table 4 we give the contributions from these discrete states to the integrated rate. We see that they are of the same order of magnitude than the continuum ones and lead to a reasonable agreement with the experimental data. To describe properly the magnitude and the position of each individual discrete transition, one would need a more sophisticated model for the residual ^{12}B, ^{16}N and ^{40}K nuclei than the one used here, as it was the case when we discussed the continuum integrated rates. However, the sum of all the discrete and continuum contributions is rather model independent as it can be seen in Table 5. Results with potentials B, C and D agree within around 4%, while the value obtained with potential A is well below the previous ones. This is because the proton well for potential A is more attractive than for the rest of potentials, and therefore the overlap between the holes and pion wave functions is smaller. Changes in the proton potential modifies both the continuum and discrete contributions, and then the total rate. However, variations of the neutron potential depth, leaving fixed the proton one, make some single–particle states to be bound or not. In this last case, low energy resonances appear in the spectrum. Thus, the net effect is an exchange of strength between the discrete and continuum contributions to the RPC rate, leaving

	$R^{(\gamma)}$ [%]			
	Shell–model			
Potential/Density	Continuum	Discrete	Total	LDA Fermi gas
A	1.17 (1.25)	0.87 (0.92)	2.04 (2.17)	2.20
B	1.44 (1.54)	0.97 (1.03)	2.41 (2.57)	2.62
C	1.76 (1.87)	0.57 (0.61)	2.33 (2.48)	2.59
D	1.14 (1.21)	1.28 (1.36)	2.42 (2.57)	2.66
2pF	–	–	–	2.74

Table 5: Comparison of the results (in percent) for $R^{(\gamma)}(q)$ in ^{40}Ca for the same potentials of the Table 3 and the FG model of Ref. [6]. In the first column we give either the Wood–Saxon potential used to compute the SM results or the proton and neutron center densities needed as input in the FG model. Densities A–D refer to those obtained from the corresponding Wood–Saxon potentials A–D and 2pF to the two parameter Fermi density used in the Ref. [6] and taken from Ref. [33]. The 2pF value does not match the one shown in Table 4 because here RPA correlations have not been included and the error bars due to uncertainties in the strong absorption widths, Γ^{abs}_{nl}, have been dropped out. To compare with the FG model we also show in brackets the results of the SM calculation without taking into account $2p2h$ correlations.

almost unchanged the total value.

From the above discussion we see that reasonable changes in the proton potential lead to about 15-20% uncertainty in the SM results. Moreover, one gets an additional 4% uncertainty associated to the neutron potential, thus we conclude that the SM gives integrated RPC rates with an uncertainty of about 20-25%. Similar results are also found for carbon and oxigen. This uncertainty is basically due to two facts: *i)* the RPC process takes place at the nuclear surface and *ii)* the main contribution to the integrated RPC rate comes from nuclear excitation energies rather low ($\approx 5-10$ MeV). For processes sensitive to the whole nuclear volume and involving larger excitation energies (see for instance calculations at the quasielastic peak for inclusive (e,e') scattering [11]) the SM results are much more independent of the details of the mean field.

4. We have not included RPA correlations in our model. In Ref. [6] RPA lead to a reduction of about 40% in the integrated ratios without changing the shape of the photon distribution. In Table 5 we compare the SM results, without including $2p2h$ correlations (in brackets), to those obtained with the LDA FG model of Ref. [6] without including RPA correlations (last row). We see that the FG model value (2.74) is significantly higher than the SM ones, part of this discrepancy being due to the use of different proton and neutron center distributions in both types of calculations. To make more reliable the comparison, we also show the LDA FG results obtained using the proton and neutron densities derived from the different Wood-Saxon potentials used in the SM calculations. We can see now that the FG

model gives similar results to those of the SM and it is also subject to the same type of uncertainties (20-25%) associated to the precise details of the nuclear dynamics. Similar results are obtained in carbon and oxygen.

However, we would like to point out that the LDA FG results are in most cases above the SM ones. This can be due to the undoubted deficiencies of the FG picture of the nucleus to describe processes where low nuclear excitation energies are involved. But one could also try to explain this disagreement (or part of it) by questioning the validity of the LDA to describe a surface process like the one studied here. In any case, because of the zero range character of the Kroll–Ruderman interaction considered here, LDA should work much better than what one could expect.

In any case, and in view of the results in Table 5, one might think that the effect of the inclusion of the RPA correlations could be similar in both models. The fact that the SM result shows an uncertainty comparable to the expected RPA effects prevents us to try to include such correlations before having a more reliable nuclear model.

4 Summary and conclusions

In this paper we have reanalyzed the RPC process in light and medium nuclei. We have presented a simple continuum SM which describes successfully the shape of the photon distribution. We have paid a special attention to the study of the low energy part of the photon spectrum which could not be fully understood within the different models found in the literature and in special in the model of Ref. [6], despite of being the only one able to describe the experimental integrated ratios $R^{(\gamma)}$ thorough the periodic table. We have found that the effect of $2p2h$ correlations play an essential role to describe the tail at low energies of the photon distribution and that these effects together with the use of nucleon wave functions with non-vanishing high momentum components allow us for a correct description of this part of the spectrum.

We have also found that the region of high photon energies depends strongly on the details of the nuclear model used. In that region when the outgoing neutron is bound, the photon spectrum exhibits peaks characteristic of the energy spectrum of the final nucleus. Also in this region, when the emitted neutron goes to the continuum, there are peaks corresponding to resonances of the final residual nucleus. Much effort have been invested in the past to extract information about these nuclear bound and resonances states [1], [2] and [10]. We think that a first necessary step to attack this interesting problem is a correct understanding of the quasifree background, studied here, which requires the inclusion of two body mechanisms and to deal with orthogonal particle-hole states. Thus, results presented in this paper could be used in future to isolated the contribution of such nuclear states from the experimental data. This would clearly represent an improvement with respect previous works where the subtraction of the quasifree background was performed by means of optical model calculations or the non-theoretical founded pole model (see Ref. [2]).

Finally, we have obtained values for the integrated ratio $R^{(\gamma)}$ in good agreement with those found with the FG model of Ref.[6]. We have also discussed different mechanisms which could account for the remaining discrepancies with the experimental data. None of them are expected to make narrower the photon distribution because, as we have mentioned above, the tail of the distribution is mainly due to $2p2h$ effects and high momentum components in the nucleon wave functions and these physical effects will be present in all new contributions to the RPC rate.

Acknowledgments

We are indebted to P. Trüol for providing us with the files containing part of the experimental data presented in this work. This research was supported by DGES under contract PB95-1204 and by the Junta de Andalucía.

Appendix
Matrix elements of the electromagnetic operators

In this appendix we give the matrix elements needed to calculate the width of the RPC process as given by Eq. (2). As it can be seen in Eq. (5), $\mathbf{J}(\mathbf{r})$ is in our case a one–body operator in the nuclear space. Thus both $T^{\rm el}_{JM}$ and $T^{\rm mag}_{JM}$ operators are also. We define the auxiliary operators $\mathcal{U}^{\rm el,mag}$ by integrating the operators $T^{\rm el,mag}$ over the pionic degrees of freedom and projecting the result onto a well defined angular momentum basis.

$$\mathcal{U}^{\rm el,mag}_{JJ_iJ'M'}(q) \equiv \left[{}_\pi\langle 0|T^{\rm el,mag}_J(q)|\pi^-;J_i\rangle\right]_{J'M'} \tag{18}$$

$$= \sum_{MM_i}\langle JMJ_iM_i|J'M'\rangle_\pi\langle 0|T^{\rm el,mag}_{JM}(q)|\pi^-;J_iM_i\rangle \tag{19}$$

where the pion states $|\pi;J_i\rangle$ and $|0\rangle_\pi$ where defined in section 2.2. The $\mathcal{U}^{\rm el,mag}_{JJ_iJ'M'}(q)$ operators act now only on nuclear states and have rank $J'M'$. The reduced matrix elements of the $T^{\rm el,mag}$ operators can be related to those of the $\mathcal{U}^{\rm el,mag}$ operators,

$$\langle ph^{-1};J_f\|T^{\rm el,mag}_J(q)\|J_i\rangle = (-1)^{J_i-J-J_f}\langle p\|\,\mathcal{U}^{\rm el,mag}_{JJ_iJ_f}(q)\,\|h\rangle, \tag{20}$$

where the particle and hole states with third isospin component t_p and t_h respectively are given by:

$$|p\rangle = R_p(r,\epsilon_p)|\frac{1}{2}\,l_p;j_pm_p\rangle|\frac{1}{2},t_p\rangle \tag{21}$$

$$|h\rangle = R_h(r,\epsilon_h)|\frac{1}{2}\,l_h;j_hm_h\rangle|\frac{1}{2},t_h\rangle. \tag{22}$$

As we discussed in sect. 2.2, the radial wave functions R_p and R_h are obtained by solving the Schrödinger equation with the potential described in that section, for positive (ϵ_p) and negative (ϵ_h) energies, respectively. The values of ϵ_h are determined by the quantum numbers n_h, l_h and j_h of the occupied shells in the parent nucleus, whereas the positive energies ϵ_p are determined by energy conservation. The particle radial wave functions R_p are normalized to the Dirac's delta of energies.

By using Eqs. (3)-(5) and Eq. (10) one can find the following expressions for the single-particle $\mathcal{U}^{\rm el,mag}_{JJ_iJ'M'}(q)$ operators:

$$\begin{aligned}
\mathcal{U}^{\rm mag}_{JJ_iJ_fM_f}(q) &= i\sqrt{2}\,\frac{f}{m_\pi}\left(1+\frac{m_\pi}{2M}\right)\frac{1}{\sqrt{2E^\pi_{nJ_i}}}t_- \qquad (23)\\
&\quad\times j_J(qr)R^\pi_{nJ_i}(r)\left[\left[Y_J(\hat{\mathbf{r}})\otimes\sigma\right]_J\otimes Y_{J_i}(\hat{\mathbf{r}})\right]_{J_fM_f}\\
\mathcal{U}^{\rm el}_{JJ_iJ_fM_f}(q) &= \sqrt{2}\,\frac{f}{m_\pi}\left(1+\frac{m_\pi}{2M}\right)\frac{1}{\sqrt{2E^\pi_{nJ_i}}}t_- \qquad (24)\\
&\quad\times\frac{1}{\hat{J}}\sum_{s=\pm1}s\sqrt{J+\delta_{s,-1}}\,j_{J+s}(qr)R^\pi_{nJ_i}(r)\left[\left[Y_{J+s}(\hat{\mathbf{r}})\otimes\sigma\right]_J\otimes Y_{J_i}(\hat{\mathbf{r}})\right]_{J_fM_f}
\end{aligned}$$

where $\mathbf{r}$ is now the nucleon spatial coordinate and $\hat{J}=\sqrt{2J+1}$.

By using Racah algebra to compute the reduced matrix elements of the operators in Eqs. (23-24) we get finally:

$$\begin{aligned}
\langle ph^{-1};J_f\|\,T^{mag}_J(q)\,\|J_i\rangle &= i\frac{f}{m_\pi}\left(1+\frac{m_\pi}{2M}\right)\frac{1}{\sqrt{E^\pi_{nJ_i}}}\frac{1}{4\pi}\delta_{t_p,-\frac{1}{2}}\delta_{t_h,\frac{1}{2}}(-1)^{j_p-1/2+J_f}\\
&\quad\times\hat{j_p}\hat{j_h}\hat{J}\hat{J}_i\hat{J}_f\xi(l_p+l_h+J+J_i)\begin{pmatrix} j_p & j_h & J_f\\ \frac{1}{2} & -\frac{1}{2} & 0\end{pmatrix}\\
&\quad\times\frac{\kappa_p+(-1)^{l_p+l_h+J_f+1}\kappa_h}{\sqrt{J_f(J_f+1)}}\begin{pmatrix} J_f & J & J_i\\ 1 & -1 & 0\end{pmatrix}\\
&\quad\times\int_0^\infty dr\,r^2R_p(r)j_J(qr)R_\pi(r)R_h(r) \qquad (25)\\
\\
\langle ph^{-1};J_f\|\,T^{el}_J(q)\,\|J_i\rangle &= \frac{f}{m_\pi}\left(1+\frac{m_\pi}{2M}\right)\frac{1}{\sqrt{E^\pi_{nJ_i}}}\frac{1}{4\pi}\delta_{t_p,-\frac{1}{2}}\delta_{t_h,\frac{1}{2}}(-1)^{j_p-1/2+J_f}\\
&\quad\times\hat{j_p}\hat{j_h}\hat{J}\hat{J}_i\hat{J}_f\xi(l_p+l_h+J+J_i+1)\begin{pmatrix} j_p & j_h & J_f\\ \frac{1}{2} & -\frac{1}{2} & 0\end{pmatrix}\\
&\quad\times\left\{\frac{\kappa_p+(-1)^{l_p+l_h+J_f+1}\kappa_h}{\hat{J}^2\sqrt{J_f(J_f+1)}}\begin{pmatrix} J & J_f & J_i\\ 1 & -1 & 0\end{pmatrix}\right.\\
&\quad\times\int_0^\infty dr\,r^2R_p(r)[Jj_{J+1}(qr)-(J+1)j_{J-1}(qr)]R_\pi(r)R_h(r)
\end{aligned}$$

$$-\sqrt{J(J+1)}\begin{pmatrix} J & J_f & J_i \\ 0 & 0 & 0 \end{pmatrix}$$
$$\times \frac{1}{q}\int_0^\infty dr\, r R_p(r) j_J(qr) R_\pi(r) R_h(r)\Bigg\}. \quad (26)$$

where we have defined $\kappa_\alpha = (l_\alpha - j_\alpha)(2j_\alpha + 1)$ and the parity function $\xi(n) = 1(0)$ for even (odd) values of n.

References

[1] J.D. Vergados, Phys. Rev. **C12** (1975) 1278

[2] H.W. Baer, K.M. Crowe and P. Trüol, Advances in nuclear physics, vol. 9, M. Baranger and E. Vogt, eds., 1977, and references therein

[3] M. Gmitro, H.R. Kissener, P. Trüol and R.A. Eramzhyan, Sov. J. Phart. Nucl. **13** (1982) 513; **14** (1983) 323

[4] F. Roig and J. Navarro, Nucl. Phys. **A440** (1985) 659

[5] H. Krivine, E. Lipparini, J. Navarro and F. Roig, Nucl. Phys. **A481** (1988) 781

[6] H.C. Chiang, E. Oset, R.C. Carrasco, J. Nieves and J. Navarro, Nucl. Phys. **A510** (1990) 573

[7] R.C. Carrasco and E. Oset, Nucl. Phys. **A536** (1990) 445; R.C. Carrasco, Ph. D Thesis, Universidad de Valencia, 1991 (unpublished)

[8] R.A. Eramzhyam, M. Gmitro, R.A. Sakaev and L.A. Tosunjan, Nucl. Phys. **A290** (1977) 294

[9] N. Ohtsuka and H. Ohtsubo, Nucl. Phys. **A306** (1978) 513

[10] R. Wünsch, Nucl. Phys. **A336** (1980) 446; J. Phys. G: Nucl. Phys. **10** (1984) 1361

[11] J.E. Amaro, G. Co' and A.M. Lallena, Ann. Phys. (N.Y.) 221 (1993) 306; J.E. Amaro, Ph.D. Thesis, Universidad de Granada, 1993 (unpublished)

[12] J.E. Amaro, G. Co' and A.M. Lallena, Nucl. Phys. **A578** (1994) 365;

[13] T. deForest and J.D. Walecka, Adv. Phys. **15** (1966) 57

[14] T.E.O. Ericson and W. Weise, *Pions and Nuclei* (Clarendon Press, Oxford, 1988)

[15] J.E. Amaro, C. García-Recio and A.M. Lallena, Nucl. Phys. **A567** (1994) 701.

[16] J. Nieves, E.Oset and C.García-Recio, Nucl. Phys. **A554** (1993) 509.

[17] J. Nieves, E.Oset and C.García-Recio, Nucl. Phys. **A554** (1993) 554.

[18] R.D. Smith and J. Wambach, Phys. Rec. **C38** (1988) 100.

[19] G.Co', K.F.Quader, R.D. Smith and J. Wambach, Nucl. Phys. **A485** (1988) 61.

[20] A. Gil, J. Nieves and E. Oset, Granada preprint: UG-DFM-2/97.

[21] G. Backentoss, Ann. Rev. Nucl. Sci. **20** (1970) 467

[22] G. de Chambrier *et al.,* Nucl. Phys. **A442** 1985) 637

[23] J. Konijn *et al.,* Nucl. Phys. **A326** (1979) 401

[24] J.F.M. d'Achard *et al.,* Phys. Lett. **B136** (1984) 24

[25] A. Olin *et al.,* Nucl. Phys. **A439** (1985) 589.

[26] G. Co', A.M. Lallena and T.W. Donnelly, Nucl. Phys. **A469** (1987) 684.

[27] J.E. Amaro *et al.,* Nucl. Phys. **A602** (1996) 263.

[28] J.A. Bistirlich, K.M. Crowe, A.S.L. Parsons, P.Skarek and P. Trüol, Phys. Rev. **C5** (1972) 1867.

[29] S. Boffi, F. Cannata, F. Capuzzi, C. Giusti and F.D. Pacati, Nucl. Phys. **A379** (1982) 509.

[30] H. Davies, H. Muirhend and J.N. Woulds, Nucl. Phys. **78** (1966) 673.

[31] V.I. Petrukhin and Y.D. Prokoshkin, Nucl. Phys. **66** (1965) 669.

[32] G. Strassner *et al.,* Phys. Rev. **C20** (1979) 248.

[33] C.W. Jagger, C. de Vries and H. de Vries, At. Data Nucl. Data Tables **14** (1974) 480.